BNL-215904-2020-JAAM

Highly stable inverted methylammonium lead tri-iodide perovskite solar cells achieved by surface re-crystallization

H. Back, C. Nam

To be published in "Energy & Environmental Science "

January 2020

Center for Functional Nanomaterials

Brookhaven National Laboratory

U.S. Department of Energy

USDOE Office of Science (SC), Basic Energy Sciences (BES) (SC-22)

Notice: This manuscript has been authored by employees of Brookhaven Science Associates, LLC under Contract No. DE-SC0012704 with the U.S. Department of Energy. The publisher by accepting the manuscript for publication acknowledges that the United States Government retains a non-exclusive, paid-up, irrevocable, world-wide license to publish or reproduce the published form of this manuscript, or allow others to do so, for United States Government purposes.

DISCLAIMER

This report was prepared as an account of work sponsored by an agency of the United States Government. Neither the United States Government nor any agency thereof, nor any of their employees, nor any of their contractors, subcontractors, or their employees, makes any warranty, express or implied, or assumes any legal liability or responsibility for the accuracy, completeness, or any third party's use or the results of such use of any information, apparatus, product, or process disclosed, or represents that its use would not infringe privately owned rights. Reference herein to any specific commercial product, process, or service by trade name, trademark, manufacturer, or otherwise, does not necessarily constitute or imply its endorsement, recommendation, or favoring by the United States Government or any agency thereof or its contractors or subcontractors. The views and opinions of authors expressed herein do not necessarily state or reflect those of the United States Government or any agency thereof.

COMMUNICATION

Highly stable inverted methylammonium lead tri-iodide perovskite solar cells achieved by surface re-crystallization

Received 00th January 20xx,
Accepted 00th January 20xx

DOI: 10.1039/x0xx00000x

Hyungcheol Back[a,b‡], Geunjin Kim[a,c‡], Heejoo Kim[a,d*], Chang-Yong Nam[e], Jinhyun Kim[f], Yong Ryun Kim[a], Taejin Kim[g], Byoungwook Park[h], James R. Durrant[f], Kwanghee Lee[a,h*]

Despite the promise of a simple manufacturing via entire solution process at low temperature (< 100 °C), the planar-type inverted perovskite solar cells (PeSCs) based on methylammonium lead tri-iodide ($MAPbI_3$) still suffer from a notorious instability problem under operational conditions. Here, we found that the operational stability of PeSCs with $MAPbI_3$ is significantly related with a high density of ionic defects and correlated amorphous regions at the interface between the electron transport layer and the $MAPbI_3$ film. By recrystailizing the surface of the $MAPbI_3$ layer, we fabricate a defect-free stoichiometric $MAPbI_3$ crystals and demonstrated burn-in loss-free and intrisically stable inverted $MAPbI_3$ PeSCs. The inverted $MAPbI_3$ PeSCs exhibited a power conversion efficiency (PCE) of 18.8% that was maintained over 80% and 90% of their initial PCEs even after 1000 hours of real operation (under AM 1.5G irradiation) and continuous heating conditions (at 85 °C in the dark), respectively. Our work demonstrates that the $MAPbI_3$ layer in an ionic defect-free condition is 'intrinsically' stable under operational condition.

The development of organic-inorganic lead halide perovskite semiconductors has sparked tremendous research on solution-processed thin-film solar cells because of their superior optoelectronic properties, such as a large exciton diffusion length, a long carrier lifetime, and a high absorption coefficient.[1-6] Therefore, the power conversion efficiency (PCE) of the perovskite solar cells (PeSCs) continues to increase, exceeding 25.2%.[7-9] Because this value is comparable to that of multicrystalline Si solar cells, the real commercialization of PeSCs is expected to be achieved soon. However, the lack of reliable operational stability of PeSCs under continuous photoirradiation or thermal stress has been a crucial barrier to this purpose.

As a consequence of huge efforts to improve the operational stability of PeSCs last few years, their stability has been widely accepted to be significantly related to the decomposition of organic parts of the perovskite, such as methylammonium halide (MAX); this inevitably causes the generation of defects in thin perovskite films, resulting in the degradation of PeSCs under continuous photoirradiation, thermal stress, oxygen, and moisture.[8-11] One considers that the MAX-based PeSCs are 'intrinsically' unstable even with proper encapsulation or under dry inert conditions, so that PeSCs undergo 'self-degradation'.[12-15] Therefore, to overcome the instability problem in the MAX-based PeSCs, two strategies have been adapted. The first approach is interfacial engineering of PeSCs by introducing perfect interfacial layers with a superior smoothness, a hydrophobic nature, and a pinhole-free morphology.[16, 17] Among these layers, graphene or a combination of graphene and copper (I) thiocyanate (CuSCN) exhibited successful protection from external and/or internal contaminants such as moisture, oxygen, and iodide ions, thus resulting in excellent stability for the mesoporous-type PeSCs.[17]

The other approach is compositional engineering of the photoactive materials, which introduces new or mixed cation systems, such as through replacement of MA with formamidinium (FA), cesium (Cs), and other cations or their mixture system in a formula of ABX_3. Because this approach results in many improvements in the material quality of the perovskite layers, including a decrease of defects, an increase of the crystal grain size, fewer pinholes on the surface, and an increase in the vertical transport in the films, a substantial enhancement in the device stability has been demonstrated.[18-20] The use of a two-dimensional (2-D)/three-dimensional (3-D) heterostructure in the perovskite material has also led to improved stability of PeSCs by passivating defect sites in the crystalline perovskite.[21-23]

Despite these successes, some issue still remains that need to be understood: the fundamental questions for the origin of the

[a]*Heeger Center for Advanced Materials & Research Institute for Solar and Sustainable Energies, Gwangju Institute of Science and Technology, Gwangju 61005, Republic of Korea,*
[b]*Hanwha Q Cells & Advanced Materials, 305 Pangyo-ro, Bundanggu, Seongnam, Gyeonggi 13488, Republic of Korea*
[c]*Division of Advanced Materials, Korea Research Institute of Chemical Technology, 141 Gajeong-Ro, Yuseong-Gu, Daejeon 34114, Republic of Korea*
[d]*Institute of Integrated Technology, Gwangju Institute of Science and Technology, Gwangju 61005, Republic of Korea, E-mail:heejook@gist.ac.kr*
[e]*Center for Functional Nanomaterials, Brookhaven National Laboratory, Upton, New York 11973, USA*
[f]*Department of Chemistry and Centre for Plastic Electronics, Imperial College London, London SW7 2AZ, United Kingdom*
[g]*Department of Materials Science and Chemical Engineering, Stony Brook University, Stony Brook, New York 11794, USA*
[h]*School of Materials Science and Engineering, Gwangju Institute of Science and Technology, Gwangju 61005, Republic of Korea, E-mail:klee@gist.ac.kr*
‡ H. Back and G. Kim contributed equally to this work.
Electronic Supplementary Information (ESI) available: [details of any supplementary information available should be included here]. See DOI: 10.1039/x0xx00000x

Please do not adjust margins

instability of MAX based PeSCs under operational condition. Because aforementioned approaches could overcome the stability issues by using the circumvent ways such as interfacial engineering, compositional engineering and, an introduction of new hetero-materials systems, a rigorous study on the intrinsic property for the degradation in MAX layer has not been fully explored. In general, the doped interlayer in the device structure, such as hole transport layer (HTL) and electron transport layer (ETL), could affect the stability of MAX layer significantly.[24] Thus, to rule out extrinsic effect from these layers, the planar-type inverted (p-i-n) PeSCs, which have undoped organic layers for HTL and ETL, would be useful (for example, Poly[bis(4-phenyl)(2,4,6-trimethylphenyl)amine] (PTAA) for HTL and a fullerene derivative, [6,6]-phenyl-C_{61} butyric acid methyl ester (PCBM) for ETL).

Here, we demonstrate that the operational stability of PeSCs based on $MAPbI_3$, which is the simplest mixture of methylammonium iodide (MAI) and lead (II) iodide (PbI_2), is significantly related with the surface stoichiometry of the perovskite layers by systematically exploring the degradation process of p-i-n planar-type inverted $MAPbI_3$ PeSCs under operational conditions; their off-stoichiometry at the surface leads to the generation of a high density of ionic defects and amorphous regions, deteriorating the operational stability of the PeSCs. Then, by applying a vacuum-assisted solid-phase recrystallization process to the $MAPbI_3$ layer with the PCBM, we were able to successfully remove the amorphous region at the surface of the $MAPbI_3$ layer, resulting in a reconstructed surface stoichiometry, approaching to an ideal stoichiometry for the $MAPbI_3$ layer. The PCBM layer holds the ionic defects extracted from the $MAPbI_3$ layer during the vacuum process and facilitates stoichiometric recrystallization of $MAPbI_3$. After subsequent removal and redeposition of the PCBM layer on the vacuum-processed $MAPbI_3$ layer, we demonstrated a long-term operational and thermal stability in the p-i-n planar-type inverted PeSCs, which maintain over 80% of their initial PCEs even after '1000 hours' of operation at their maximum power point (MPP) under full air mass 1.5 global (AM 1.5G) irradiation (Xe lamp without a UV cutoff filter) and retain 90% of their initial PCEs after '1000 hours' of storage at 85 °C under inert nitrogen (N_2) gas conditions. Therefore, we demonstrate that the $MAPbI_3$ perovskite layer in an ionic defect-free condition has 'intrinsically' excellent operational stability and thermal stability.

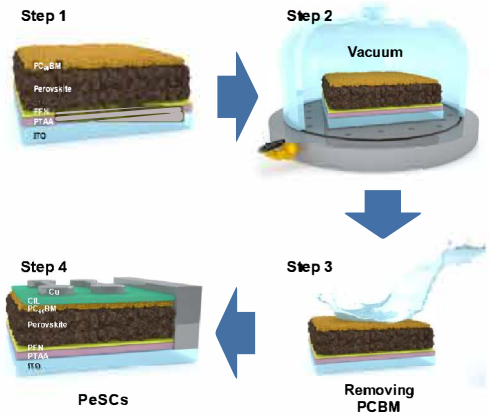

Figure 1 | The fabrication process of VCRP perovskite solar cells.

Device Structure and Vacuum Curing and Redeposition of PCBM (VCRP) Process

The structure of the p-i-n planar-type inverted PeSCs based on $MAPbI_3$ for this work is illustrated in Fig. 1 (a). PTAA is used as the HTL, while the ETL is a PCBM/titanium suboxide (TiO_x) bilayer. To increase the wettability of the $MAPbI_3$ solution on the PTAA layer, poly[(9,9-bis(3'-(N,N-dimethylamino)propyl)-2,7-fluorene)-alt-2,7-(9,9-dioctylfluorene)] (PFN) is used as an interfacial compatibilizer.[25] As previously reported, during the PeSC aging process, the excess defects inside the $MAPbI_3$ layer inevitably migrate to the top electrode, leading to the deterioration of the PeSC interface and gradually reduced device performance even under dark and inert N_2 gas storage conditions.[14, 26] Furthermore, this migration of ionic defects in the PeSCs can be accelerated by an external electrical and/or light bias, which causes extremely fast degradation of the device performance within several hours, a phenomenon typically referred to as, burn-in loss.[27, 28] To simulate the burn-in loss process, we degraded the performance of PeSCs by using maximum power point tracking (MPPT) measurements under continuous AM 1.5G irradiation for 20 hours in the inert N_2 gas condition (see Fig. S1). As shown in Table S1, the parameters of PeSCs that are mainly degraded under continuous irradiation are the short-circuit current density (J_{sc}) and the fill factor (FF), in which their degradation can be originated from damages of the perovskite layer and/or interfaces with iodide ion diffused from the degraded perovskite layer within 100 hours (Fig S2). Therefore, to clarify the origin of the degradation of PeSCs, we removed the upper layers (i.e., the PCBM/TiO_x bilayer and metal electrode) and redeposited them (Fig. S3). Surprisingly, in the redeposited devices, we found that the performance of the aged device was recovered after this reconstruction process and that the decay rate (%/hour) was dramatically reduced as the redeposition process was repeated. This observation implies a reduction of the burn-in process as the number of reconstruction processes increases (see the normalized MPPT curve in the inset of Fig. S1 and Table S1). In other words, the origin of the burn-in process in PeSCs is effectively suppressed by replacing the upper interfacial layers, and the interface of the perovskite layer is stabilized by reducing the defects at the interface.

To clarify the redeposition effect of the devices, we tested MPPT on the redeposition-only PeSC (a redeposition of a fresh PCBM on the pristine $MAPbI_3$/PCBM layer). Comparing to the pristine device, the operational stability of the redeposition-only device was slightly improved despite fast burn-in process with large decay rates (an operation time to 80% of the initial PCEs) of 10%/h (13%/h for pristine device) (Fig. S4). However, a case with a vacuum-only processed device (depositing PCBM on vacuum processed $MAPbI_3$ layer) exhibits delayed burn-in degradation with the rate of 0.33%/h. To investigate this different behaviour in the stability for above devices, we conducted X-ray photoelectron spectroscopy (XPS) on the surfaces of the $MAPbI_3$ and we found that nitrogen (N) and lead (Pb) atom at the surface of pristine $MAPbI_3$ and the redeposition processed $MAPbI_3$ are mismatched with N/Pb = 0.84 for the pristine and 0.88 for the redeposition only $MAPbI_3$ layer, respectively. In contrast, as we expected, the vacuum-only processed case shows a matched ratio of 0.99 (Fig. S5). Despite the improvement of the operational stability with vacuum process of $MAPbI_3$ layer, the devices still exhibit burn-in degradation within a hundred hour.

The significant improvement in the operational stability is observed in the device with vacuum processed film of $MAPbI_3$/PCBM. As shown in Fig. S6, this device exhibited the significant decrease of decay rate (0.20%/h). In contrast to the above cases, this additional improvement cannot be interpreted with the relation between the fast decay rate and the atomic ratio as shown in Fig. S6 b. However, this result indicates that the vacuum process with PCBM can be a key to solve the burn-in loss problem

Please do not adjust margins

of the $MAPbI_3$ based PeSCs. Therefore, we assumed that the operational stability of PeSCs is significantly related with matching stoichiometry of $MAPbI_3$ layer and removing defects inside the active layer; the halide defects inside the stoichiometrically and structurally imperfect perovskite layer migrate to the interlayers, which can subsequently capture defects. Furthermore, it also means that a certain environment for stabilizing the perovskite layer and a refreshing process by removing the damaged interface between PeSCs and interlayer can overcome the fast burn-in loss of the PeSCs.

To stabilize the perovskite layer and minimize the interaction between the two layers, we developed a vacuum curing and redeposition of PCBM (VCRP) method. Our VCRP process consists of (1) preparing PCBM-deposited perovskite film on an indium-tin oxide (ITO)/PTAA/PFN substrate, (2) maintaining this film under high vacuum conditions (< 10^{-6} torr) for over 100 hours, (3) removing the PCBM layer using an organic solvent, and (4) completing device fabrication with a redeposited PCBM layer, as illustrated in Fig. 1a.

Photovoltaic Performance of the VCRP Devices

Our VCRP devices exhibit a reasonable device performance without significant degradation compared to the reference device (Fig. S7 and Table S2), and hysteresis behaviours were negligible (Figs. S7 and S8) within 7%. After confirming the performance of our VCRP devices, we measured the long-term operational photostability of VCRP PeSCs under operational conditions using the MPPT method (Figs. S9-S11) as well as their thermal stability under storage at 85 °C in the dark for 1000 hours. In addition, to exclude any undesirable effect, the MPPT method and the storage test at 85 °C were carried out in a N_2-filled glove box without a UV filter and any encapsulation.

Fig. 2a exhibits the long-term stabilities of VCRP PeSCs under operational (Fig. 2a top) conditions and under continuous thermal exposure (Fig. 2a bottom) conditions, respectively. After 1000 hours, the PCEs of VCRP PeSCs are maintained at 80% (continuous operation under AM 1.5 illumination, as directly determined by MPPT) and 90% (continuous heating condition at 85 °C) of their pristine performances. Compared with the pristine devices, a burn-in loss-free behaviour can be observed for VCRP PeSCs in their initial stage with negligible degradation of J_{sc} and an open-circuit voltage (V_{oc}) (Fig. S11 and S12). Surprisingly, we observed that the aged VCRP PeSC (i.e., 2nd VCRP PeSC) with reconstructed PCBM layer and electrode exhibited a recovered J_{sc} value of 20.31 mA cm^{-2} (the J_{sc} values for the initial device and 1000-hour aged VCRP PeSC are 19.78 mA cm^{-2} and 17.82 mA cm^{-2}, respectively, as shown in Fig. S12 and Table S3). These results indicate that the bulk properties of the perovskite layer (such as, absorption and charge generation) are reversible even after the real operation condition under light and electrical bias.

To date, although several reports have shown excellent long-term operational stability (> 1000 hours) the mixed cation/halide based PeSCs,[17, 23, 29] they also stated fast burn-in degradation process even for the operation in an inert condition or encapsulated cases; only after introducing additional passivation methods, such as adding 2D materials or inorganic passivating interlayer, their operational stabilities have been improved. Moreover, under thermal stress, despite the decrease of the FF (from 0.77 to 0.65 after continuous thermal exposure for 1000 hours) of the VCRP PeSCs, unchanged values for both J_{sc} and V_{oc} are observed, as shown in Fig. 2c.

Crystalline Structure of VCRP PeSCs

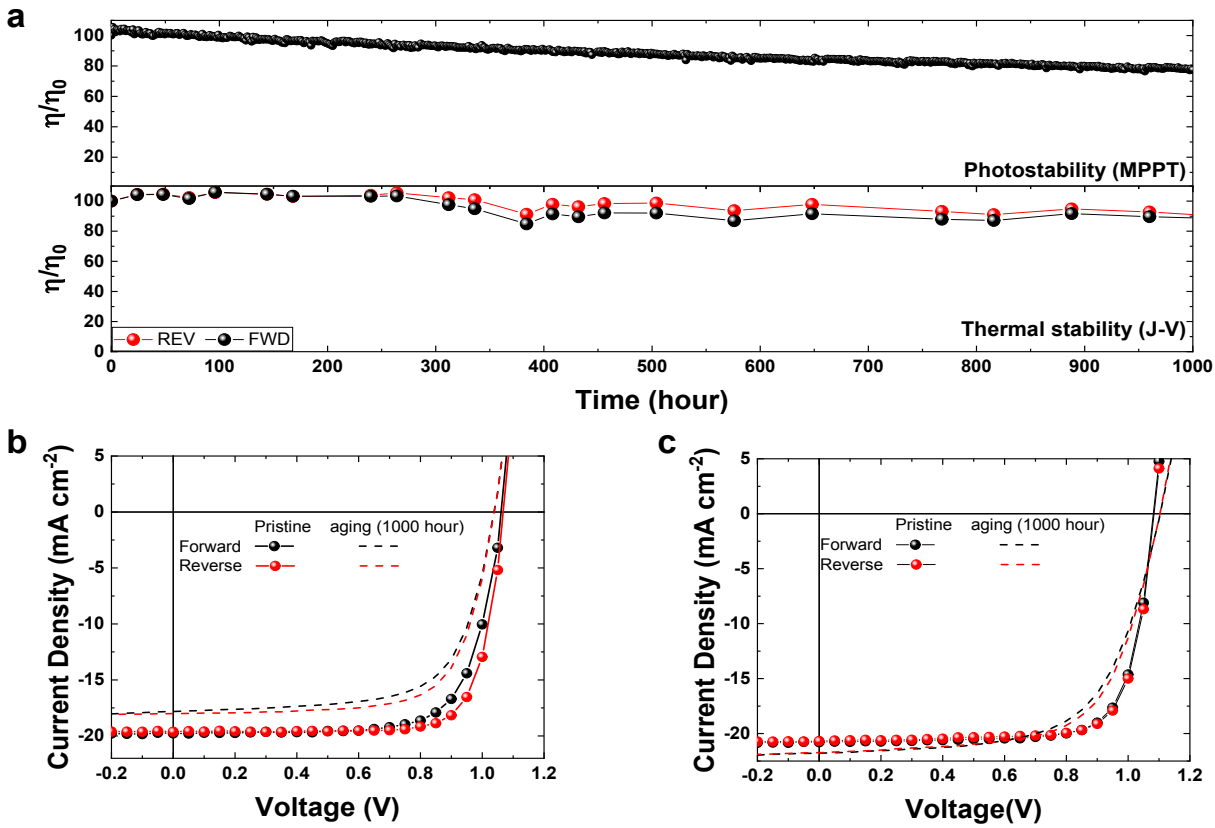

Figure 2 | J-V, Operational and Thermal stability measurements. (a) Continuous maximum power point (MPP) tracking for 1000 hours of unencapsulated VCRP perovskite solar cells in N2-filled glove box under continuous full-sun illumination without cutoff UV filter (top). thermal stability for 1000 hours at 85 °C of VCRP perovskite solar cells in N_2-filled glove box, PCE values taken from *J-V* scans every 24 hours (down). **(b)** *J-V* curve of VCRP perovskite solar cells before and after operational aging. **(c)** *J-V* curve of VCRP perovskite solar cells before and after thermal aging.

Please do not adjust margins

Please do not adjust margins

To clarify the effect of the VCRP process on the crystalline structure at the surface of the $MAPbI_3$ layer, we carried out grazing-incidence wide-angle X-ray scattering (GIWAXS) measurements at each step of the PeSC VCRP process: on pristine $MAPbI_3$ films, $MAPbI_3$/PCBM films, vacuum-cured $MAPbI_3$/PCBM films, and a processed $MAPbI_3$ film, which was prepared by removing the PCBM layer from the vacuum-cured $MAPbI_3$/PCBM film. GIWAXS measurements were performed at the Complex Materials Scattering (CMS, 11-BM) beamline of the National Synchrotron Light Source II at Brookhaven National Laboratory (Figs. S13 and S14). To assess the difference between the surface and bulk crystallinities of the $MAPbI_3$ layer obtained with the VCRP method, the samples were analysed at two different X-ray incidence angles, each probing surface and entire bulk of films, respectively: 0.1 degrees (surface) and 0.3 degrees (bulk) as shown in Note S2 and Fig S15. Fig. 3 presents 2-D GIWAXS pattern images (a, c) and corresponding circular averages (b, d) for the samples. The neat $MAPbI_3$ film exhibits a strong crystalline nature with several noticeable peaks at approximately 1.0 $Å^{-1}$ (110 peak of the $MAPbI_3$ film) and 2.0-2.5 $Å^{-1}$ as shown in Figs. 3b, S16 and S17.[30, 31] In addition, we can recognize a broad amorphous peak at approximately 1.5-2.5 $Å^{-1}$ (even after the background subtraction and profile normalization) and a weak peak at approximately 0.6 $Å^{-1}$, arising from an intermediate phase of $MAPbI_3$.[30] Although GIWAXS cannot elucidate which part of the $MAPbI_3$ film contributes amorphous region,[32] this result implies that the surface of the pristine $MAPbI_3$ film has a mixed state of well-crystalline perovskite crystals and amorphous regions, including decomposed states of $MAPbI_3$. The same feature is observed in the $MAPbI_3$/PCBM layer, with a slightly decreased peak intensity at 0.6 $Å^{-1}$. However, after the vacuum curing process is applied to the $MAPbI_3$/PCBM film, we found a dramatic change in the GIWAXS pattern: the disappearance of the intermediate and amorphous peaks (see Fig. 3b). In addition, a clearer peak was observed at approximately the 1.0 $Å^{-1}$ position.

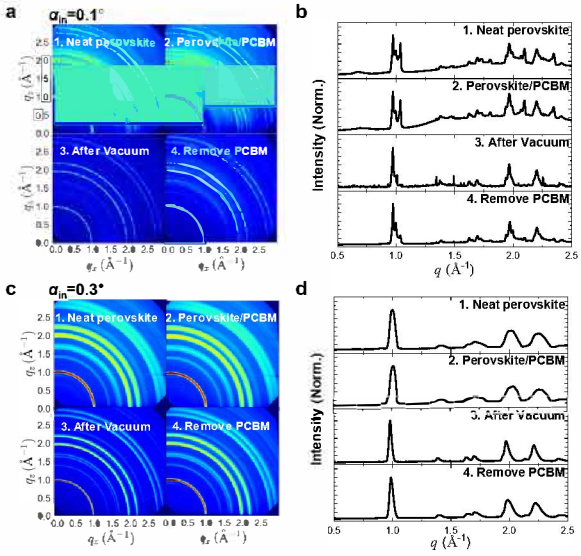

Figure 3 | GIWAXS. 2-D GIWAXS image and circular average of **(a, b)** surface crystallinity and **(c, d)** bulk crystallinity of perovskite films. After removing the PCBM layer from the vacuum-cured $MAPbI_3$/PCBM film, the same GIWAXS pattern was observed.

To clarify the vacuum curing effect on the $MAPbI_3$/PCBM film, GIWAXS measurements were carried out on a vacuum-cured $MAPbI_3$ film without PCBM atop. Interestingly, as shown in Figs. S18-20, the GIWAXS pattern for the vacuum-cured $MAPbI_3$ film is almost same as that for the neat $MAPbI_3$ film without the vacuum curing process. In addition, we observed two distinct features between neat $MAPbI_3$ and the VCRP sample: (1) without the vacuum curing process, just a washing PCBM process does not reduce the amorphous phase in the $MAPbI_3$ (Fig. S17). (2) in the case of a vacuum processed neat $MAPbI_3$, the amorphous phase still remained (Figs. S19c and d and Figs. S20c and d), which is absent in the vacuum-cured $MAPbI_3$/PCBM film (Fig. 3b). This result implies that the surface of the $MAPbI_3$ film is extremely unstable, thus causing a deterioration of the surface of the $MAPbI_3$ film even under vacuum process. Furthermore, the vacuum curing process applied to the structure of the $MAPbI_3$/PCBM film is effective in achieving a well-crystalline surface in the $MAPbI_3$ film. Because Lewis acid materials such as PCBM are a good acceptor of negatively charged ionic defects, such as PbI_3^- or I^-,[8, 33, 34] the ionic defects extracted from the $MAPbI_3$ film can be easily captured by the PCBM layer. Furthermore, this PCBM layer, including ionic defects, induces a surface reconstruction of the $MAPbI_3$ film during the vacuum curing process, resulting in a well-crystalline surface in the vacuum-cured $MAPbI_3$/PCBM films, as shown in Fig. 3b.

In contrast, the bulk crystalline structure of the $MAPbI_3$/PCBM film exhibits no significant change in the GIWAXS patterns before and after the vacuum curing process (Figs. 3c and d). However, we observed slight changes in the peak position and the full width at half maximum (FWHM) of the circular averages for the GIWAXS patterns; the 110 peak at q = 1.0 $Å^{-1}$ is slightly shifted to a lower angle at q = 0.98 $Å^{-1}$, and the FWHM of the corresponding peak decreases from 0.050 $Å^{-1}$ to 0.038 $Å^{-1}$ after the VCRP process (Fig. 3d and Table S5). These results imply that the vacuum curing process applied to the $MAPbI_3$/PCBM film leads to a slight expansion of crystalline $MAPbI_3$ and an increase in its mean size in the bulk film, respectively.[35]

Surface Reconstruction of VCRP PeSCs

To evaluate the morphological change of the $MAPbI_3$ film that occurs during the VCRP method, we carried out atomic force microscopy (AFM) measurements on the $MAPbI_3$ and VCRP $MAPbI_3$ films. As presented in Figs. 4a and b, we observed granules with smaller sizes in the VCRP $MAPbI_3$ film compared to the $MAPbI_3$ film. This result indicates that the surface of the VCRP $MAPbI_3$ film is reconstructed; thus, a change in the stoichiometry of the Pb:N:I atomic ratio at the surface of the $MAPbI_3$ film during the VCRP process is expected. To verify this expectation, we carried out X-ray photoelectron spectroscopy (XPS) on the surfaces of the $MAPbI_3$ and VCRP $MAPbI_3$ films. For the VCRP $MAPbI_3$ film, the PCBM layer was removed before performing XPS measurements. As shown in Fig. S21 and Table S6, the surface of the pristine $MAPbI_3$ film shows an atomic ratio of 1.00:0.84:2.83 corresponding to Pb:N:I, which means the atomic ratio for Pb and N is inadequate compared to ideal ratio.

However, rearrangement of the Pb:N:I atomic ratio is observed to occur at the interface of the VCRP $MAPbI_3$ film; the stoichiometry of the Pb:N:I atomic ratio is 1.00:1.04:3.30, which approaches the ideal stoichiometry of crystalline $MAPbI_3$. Therefore, we infer that rearrangement of the stoichiometry at the surface of the VCRP $MAPbI_3$ film can be achieved by reducing mobile iodide ions (I^-) and stabilizing $CH_3NH_3^+$ (MA^+) ions through the recrystallization of the amorphous surface of the perovskite film during the VCRP process.

Please do not adjust margins

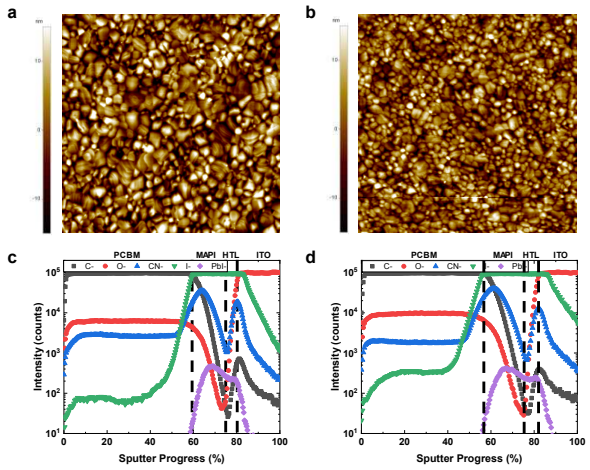

Figure 4 | AFM image and depth-profile XPS of perovskite films. AFM images of **(a)** pristine perovskite and **(b)** VCRP processed perovskite. Time-of-flight secondary ion mass spectroscopy of **(c)** pristine perovskite/PCBM and **(d)** VCRP processed-redeposited perovskite/PCBM.

To obtain more detailed information on the reconstructed surface of the VCRP $MAPbI_3$ film, we carried out time-of-flight secondary ion mass spectrometry (ToF-SIMS) and XPS depth profiling on the $MAPbI_3$/PCBM and VCRP $MAPbI_3$/PCBM films. As shown in the ToF-SIMS depth profile for the $MAPbI_3$/PCBM and VCRP $MAPbI_3$ films (Figs. 4 c-d and Figs. S22 and S23), the iodide elements (I^-) diffuse from $MAPbI_3$ to PCBM even in the pristine $MAPbI_3$/PCBM film. However, comparing the results in Fig. S22, different distributions of I^- are observed; in the VCRP $MAPbI_3$ film, the decay rate for I^- from the $MAPbI_3$ layer to the PCBM layer is slightly lower than that of the $MAPbI_3$ film. Based on this result, we speculate that slow diffusion of iodide into the PCBM layer occurred in the VCRP $MAPbI_3$ film during the vacuum curing process (Fig. S24). Furthermore, in contrast to the pristine $MAPbI_3$ film, because the PCBM scavenging layer contains iodide ions, which are extracted from the grain boundaries in the $MAPbI_3$ layer, these excess iodide ions may contribute to the rearrangement of the stoichiometry at the interface of the VCRP $MAPbI_3$ film, as observed in the XPS data. Therefore, it can be hypothesized that the VCRP process applied to the $MAPbI_3$/PCBM film leads to the evolution of a well-crystalline surface with significant reduction of amorphous regions through the extraction of ionic defects from the $MAPbI_3$ film (GIWAXS and ToF-SIMS data). Additionally, because of the ionic defects extracted from grain boundaries and/or the large-size $MAPbI_3$ crystals and excess iodide ions from the PCBM layer, large-size crystals are reduced, and amorphous regions may transform to crystals (Fig. 4e), resulting in small-size granules in the VCRP $MAPbI_3$ film, as observed in the AFM images.

Charge Dynamics of VCRP PeSCs

Because of the reduced structural defects in the VCRP $MAPbI_3$ film, different charge dynamics can be expected in the $MAPbI_3$ and VCRP $MAPbI_3$ films. Therefore, we conducted time-correlated single-photon counting (TCSPC) on the perovskite films and transient photovoltage (TPV) and impedance spectroscopy (IS) on the PeSCs. As shown in Figs. 5, the TCSPC data (Fig. 5a) clearly exhibit two phases typically assigned to fast trapping process (~ 1 ns) and slower recombination/charge transfer processes (>10 ns).[36,37] It is apparent that the VCRP process results in a reduction in the amplitude of the fast phase relative to the slow phase, consistent with this process passivating trap states at grain boundaries as discussed above.[36-38]

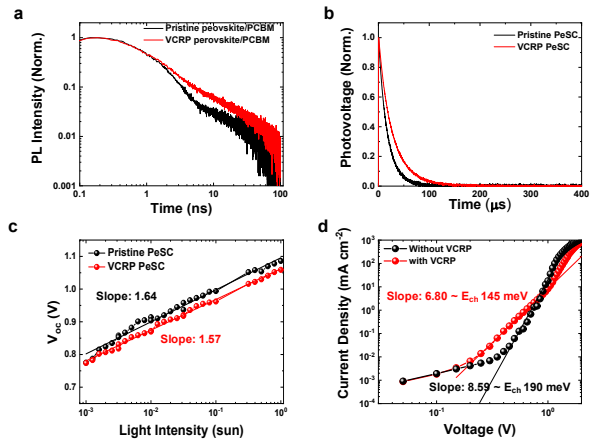

Figure 5 | Characterization of VCRP processed perovskite films and devices. (a) Time-correlated single-photon counting (TCSPC) of perovskite films. **(b)** Transient photovoltage of PeSCs (under 0.01 sun illumination). **(c)** Open-circuit voltage (V_{OC})-light intensity plot of PeSCs. **(d)** *J-V* characteristics of electron-only devices (ITO/PCBM/TiO_x/pristine or VCRP processed $MAPbI_3$/PCBM/TiO_x/Al) and their characteristic energy (E*ch*).

The difference in charge recombination lifetime of real devices was confirmed using TPV decay measurements. As shown in Fig. 5b, the VCRP-processed device exhibits a longer charge recombination lifetime (27.8 μs) compared to the control device (17.5 μs).[39] The dependence of V_{oc} on the light intensity shows a decreased V_{oc}-light intensity slope from 1.64 (pristine PeSC) to 1.57 k_BT/q (VCRP PeSC), where k_B is the Boltzmann constant, T is the temperature, and q is the elementary charge, as shown in Fig. 5c; this result represents reduced trap-assisted recombination in the VCRP PeSC, which is consistent with the TCSPC measurement result.[40] However, the energy disorder profiles of both devices obtained from light-dependent IS exhibit similar values (~ 90 meV). Therefore, the difference in the energy disorder in the PCBM layer of the pristine PeSC and VCRP PeSC can be inferred to be negligible (Fig. S25).[41] In contrast, because of the reduced ionic defects at the surface of the $MAPbI_3$ layer due to the VCRP process, the deep-trap widths of the perovskite layer decrease from 190 meV to 145 meV, as derived from the linear slopes of the *J-V* characteristics of electron-only devices (from 8.59 to 6.80) shown in Fig. 5d.[42]

Photovoltaic Performance of 1cm² PeSCs

Figures 6a and 6b show the *J-V* characteristics and incident photon-to-current efficiency (IPCE) spectrum of our optimized VCRP device (area of 0.0464 cm^2) with V_{oc} of 1.12 V, a J_{sc} of 21.63 mA cm^{-2}, and a FF of 77.9% (a corresponding PCE of 18.89% for both the reverse and forward biases). We also fabricated a larger (1 cm^2) PeSC (V_{oc} of 1.11 V, a J_{sc} of 21.41 mA cm^{-2}, and a FF of 67.8%) and conducted MPPT test under the same full operation condition of AM 1.5G irradiation with the inert N_2 condition. The device exhibited operational stability without burn-in process and maintained over than the 80% of the initial PCE during the 600-hour operation (Fig. 6c).

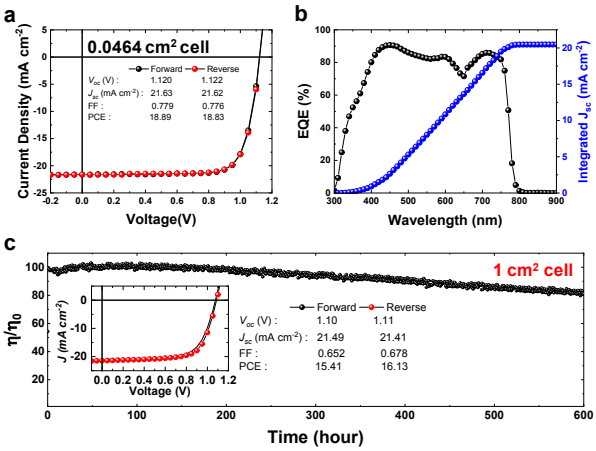

Figure 6 | Photovoltaic properties of PeSCs and MPPT of 1 cm^2-area device. (**a**) *J-V* characteristics of optimized VCRP perovskite solar cells. (**b**) EQE spectrum and J_{sc} integrated from the EQE spectrum of the best-performing VCRP perovskite solar cells and **(c)** Continuous MPP tracking for 600 hours of unencapsulated VCRP PeSC (1 cm^2 area) in N_2-filled glove box under continuous full-sun illumination without cutoff UV filter.

Conclusions

We found that a nonstoichiometric amorphous phase exists on the surface of the $MAPbI_3$ film in its as-cast state and confirmed that such imperfections lead to the fast burn-in degradation of the performance of MA-based PeSCs under operational conditions. Based on these observations, we developed a new method to reconstruct a stoichiometric crystal structure at the surface of the $MAPbI_3$ film and demonstrated burn-in loss-free planar-type inverted PeSCs with a long-term operational and thermal stability. Our reconstructed devices maintained over 80% of the initial PCEs even after '1000 hours' of operation at their maximum power point under 1 sun irradiation without a UV cutoff filter and 90% of the initial PCEs after '1000 hours' of storage at 85 °C under inert gas conditions. Finally, to evaluate the possible use of our VCRP process for large-area devices, we successfully fabricated large-area (1 cm^2) VCRP PeSCs. Our results imply that *'Stoichiometric $MAPbI_3$ is intrinsically stable'* and provide a fundamental importance and ground- breaking information to the perovskite research field, and also solve the critical lifetime issues of the PeSCs with a new defect self-healing concept.

Conflicts of interest

There are no conflicts to declare.

Acknowledgements

We thank the Heeger Center for Advanced Materials (HCAM) at the Gwangju Institute of Science and Technology (GIST) of Korea for help with device fabrication and measurements. This research was supported by the Global Research Laboratory Program of the National Research Foundation of Korea (NRF) funded by the Ministry of Science, ICT and Future Planning (NRF-2017K1A12013153). K. L. also acknowledges support provided by the GIST Research Institute (GRI) grant funded by the GIST in 2019. In addition, H.K. acknowledges the financial support from the Basic Science Research Program through the NRF funded by the Ministry of Science and ICT (NRF-2017R1A2B4012490). In addition, this research used the 11-BM Complex Materials Scattering (CMS) beamline and other resources of the National Synchrotron Light Source II and the Center for Functional Nanomaterials, which are U.S. DOE Office of Science Facilities, at Brookhaven National Laboratory under Contract No. DE-SC0012704. We thank Drs. Kevin G. Yager and Xiao Tong for their assistance with GIWAXS and XPS depth-profiling experiments, respectively.

References

1. H.-S. Kim, C.-R. Lee, J.-H. Im, K.-B. Lee, T. Moehl, A. Marchioro, S.-J. Moon, R. Humphry-Baker, J.-H. Yum, J. E. Moser, M. Grätzel and N.-G. Park, *Sci. Rep.*, 2012, **2**, 591.
2. S. D. Stranks, G. E. Eperon, G. Grancini, C. Menelaou, M. J. P. Alcocer, T. Leijtens, L. M. Herz, A. Petrozza and H. J. Snaith, *Science*, 2013, **342**, 341-344.
3. D. W. de Quilettes, S. M. Vorpahl, S. D. Stranks, H. Nagaoka, G. E. Eperon, M. E. Ziffer, H. J. Snaith and D. S. Ginger, *Science*, 2015, **348**, 683-686.
4. G. Xing, N. Mathews, S. Sun, S. S. Lim, Y. M. Lam, M. Grätzel, S. Mhaisalkar and T. C. Sum, *Science*, 2013, **342**, 344-347.
5. Q. Dong, Y. Fang, Y. Shao, P. Mulligan, J. Qiu, L. Cao and J. Huang, *Science*, 2015, **347**, 967-970.
6. S. De Wolf, J. Holovsky, S.-J. Moon, P. Löper, B. Niesen, M. Ledinsky, F.-J. Haug, J.-H. Yum and C. Ballif, *J. Phys. Chem. Lett.*, 2014, **5**, 1035-1039.
7. Best Research-Cell Efficiencies, https://www.nrel.gov/pv/assets/pdfs/best-research-cell-efficiencies.20191105.pdf, (accessed 2019-11-05).
8. X. Zheng, B. Chen, J. Dai, Y. Fang, Y. Bai, Y. Lin, H. Wei, Xiao C. Zeng and J. Huang, *Nat. Energy*, 2017, **2**, 17102.
9. N. J. Jeon, H. Na, E. H. Jung, T.-Y. Yang, Y. G. Lee, G. Kim, H.-W. Shin, S. Il Seok, J. Lee and J. Seo, *Nat. Energy*, 2018, **3**, 682-689.
10. M. Alsari, A. J. Pearson, J. T.-W. Wang, Z. Wang, A. Montisci, N. C. Greenham, H. J. Snaith, S. Lilliu and R. H. Friend, *Sci. Rep.*, 2018, **8**, 5977.
11. A. J. Pearson, G. E. Eperon, P. E. Hopkinson, S. N. Habisreutinger, J. T.-W. Wang, H. J. Snaith and N. C. Greenham, *Adv. Energy Mater.*, 2016, **6**, 1600014.
12. T. Leijtens, G. E. Eperon, S. Pathak, A. Abate, M. M. Lee and H. J. Snaith, *Nat. Commun.*, 2013, **4**, 2885.
13. G. Niu, X. Guo and L. Wang, *J. Mater. Chem. A*, 2015, **3**, 8970-8980.
14. D. Bryant, N. Aristidou, S. Pont, I. Sanchez-Molina, T. Chotchunangatchaval, S. Wheeler, J. R. Durrant and S. A. Haque, *Energy Environ. Sci.*, 2016, **9**, 1655-1660.
15. B. Conings, J. Drijkoningen, N. Gauquelin, A. Babayigit, J. D'Haen, L. D'Olieslaeger, A. Ethirajan, J. Verbeeck, J. Manca, E. Mosconi, F. D. Angelis and H.-G. Boyen, *Adv. Energy Mater.*, 2015, **5**, 1500477.
16. Y. C. Kim, T. Y. Yang, N. J. Jeon, J. Im, S. Jang, T. J. Shin, H. W. Shin, S. Kim, E. Lee, S. Kim, J. H. Noh, S. I. Seok and J. Seo, *Energy Environ. Sci.*, 2017, **10**, 2109-2116.
17. N. Arora, M. I. Dar, A. Hinderhofer, N. Pellet, F. Schreiber, S. M. Zakeeruddin and M. Grätzel, *Science*, 2017, **358**, 768-771.
18. M. Saliba, T. Matsui, J.-Y. Seo, K. Domanski, J.-P. Correa-Baena, M. K. Nazeeruddin, S. M. Zakeeruddin, W. Tress, A. Abate, A. Hagfeldt and M. Grätzel, *Energy Environ. Sci.*, 2016, **9**, 1989-1997.
19. M. Saliba, T. Matsui, K. Domanski, J.-Y. Seo, A. Ummadisingu, S. M. Zakeeruddin, J.-P. Correa-Baena, W. R. Tress, A. Abate, A. Hagfeldt and M. Grätzel, *Science*, 2016, DOI: 10.1126/science.aah5557.
20. A. D. Jodlowski, C. Roldán-Carmona, G. Grancini, M. Salado, M. Ralaiarisoa, S. Ahmad, N. Koch, L. Camacho, G. de Miguel and M. K. Nazeeruddin, *Nat. Energy*, 2017, **2**, 972-979.
21. Y. Cho, A. M. Soufiani, J. S. Yun, J. Kim, D. S. Lee, J. Seidel, X. Deng, M. A. Green, S. Huang and A. W. Y. Ho-Baillie, *Adv. Energy Mater.*, 2018, **8**, 1703392.
22. J.-W. Lee, Z. Dai, T.-H. Han, C. Choi, S.-Y. Chang, S.-J. Lee, N. De Marco, H. Zhao, P. Sun, Y. Huang and Y. Yang, *Nat. Commun.*, 2018, **9**, 3021.
23. Z. Wang, Q. Lin, F. P. Chmiel, N. Sakai, L. M. Herz and H. J. Snaith, *Nat. Energy*, 2017, **2**, 17135.
24. T. A. Berhe, W.-N. Su, C.-H. Chen, C.-J. Pan, J.-H. Cheng, H.-M. Chen, M.-C. Tsai, L.-Y. Chen, A. A. Dubale and B.-J. Hwang, *Energy Environ. Sci.*, 2016, **9**, 323-356.
25. J. Lee, H. Kang, G. Kim, H. Back, J. Kim, S. Hong, B. Park, E. Lee and K. Lee, *Adv. Mater.*, 2017, **29**, 1606363.
26. H. Back, G. Kim, J. Kim, J. Kong, T. K. Kim, H. Kang, H. Kim, J. Lee, S. Lee and K. Lee, *Energy Environ. Sci.*, 2016, **9**, 1258-1263.
27. G. Y. Kim, A. Senocrate, T.-Y. Yang, G. Gregori, M. Grätzel and J. Maier, *Nat. Mater.*, 2018, **17**, 445-449.
28. K. Domanski, B. Roose, T. Matsui, M. Saliba, S.-H. Turren-Cruz, J.-P. Correa-Baena, C. R. Carmona, G. Richardson, J. M. Foster, F. De Angelis, J. M. Ball, A. Petrozza, N. Mine, M. K. Nazeeruddin, W. Tress, M. Grätzel, U. Steiner, A. Hagfeldt and A. Abate, *Energy Environ. Sci.*, 2017, **10**, 604-613.
29. G. Grancini, C. Roldán-Carmona, I. Zimmermann, E. Mosconi, X. Lee, D. Martineau, S. Narbey, F. Oswald, F. De Angelis, M. Graetzel and M. K. Nazeeruddin, *Nat. Commun.*, 2017, **8**, 15684.

30. N.-K. Kim, Y. H. Min, S. Noh, E. Cho, G. Jeong, M. Joo, S.-W. Ahn, J. S. Lee, S. Kim, K. Ihm, H. Ahn, Y. Kang, H.-S. Lee and D. Kim, *Sci. Rep.*, 2017, **7**, 4645.
31. P. Müller-Buschbaum, *Adv. Mater.*, 2014, **26**, 7692-7709.
32. G. W. P. Adhyaksa, S. Brittman, H. Āboliņš, A. Lof, X. Li, J. D. Keelor, Y. Luo, T. Duevski, R. M. A. Heeren, S. R. Ellis, D. P. Fenning and E. C. Garnett, *Adv. Mater.*, 2018, **30**, 1804792.
33. Y. Shao, Z. Xiao, C. Bi, Y. Yuan and J. Huang, *Nat. Commun.*, 2014, **5**, 5784.
34. J. Xu, A. Buin, A. H. Ip, W. Li, O. Voznyy, R. Comin, M. Yuan, S. Jeon, Z. Ning, J. J. McDowell, P. Kanjanaboos, J.-P. Sun, X. Lan, L. N. Quan, D. H. Kim, I. G. Hill, P. Maksymovych and E. H. Sargent, *Nat. Commun.*, 2015, **6**, 7081.
35. C. Bi, Q. Wang, Y. Shao, Y. Yuan, Z. Xiao and J. Huang, *Nat. Commun.*, 2015, **6**, 7747.
36. N. D. Pham, V. T. Tiong, P. Chen, L. Wang, G. J. Wilson, J. Bell and H. Wang, *J. Mater. Chem. A*, 2017, **5**, 5195-5203.
37. J. Kim, R. Godin, S. D. Dimitrov, T. Du, D. Bryant, M. A. McLachlan and J. R. Durrant, *Adv. Energy Mater.*, **0**, 1802474.
38. Y. Yamada, T. Yamada, A. Shimazaki, A. Wakamiya and Y. Kanemitsu, *J. Phys. Chem. Lett.*, 2016, **7**, 1972-1977.
39. D. Kiermasch, P. Rieder, K. Tvingstedt, A. Baumann and V. Dyakonov, *Sci. Rep.*, 2016, **6**, 39333.
40. T. S. Sherkar, C. Momblona, L. Gil-Escrig, J. Ávila, M. Sessolo, H. J. Bolink and L. J. A. Koster, *ACS Energy Lett.*, 2017, **2**, 1214-1222.
41. Y. Shao, Y. Yuan and J. Huang, *Nat. Energy*, 2016, **1**, 15001.
42. M. M. Mandoc, B. de Boer, G. Paasch and P. W. M. Blom, *Phys. Rev. B*, 2007, **75**, 193202.

Table of Contents

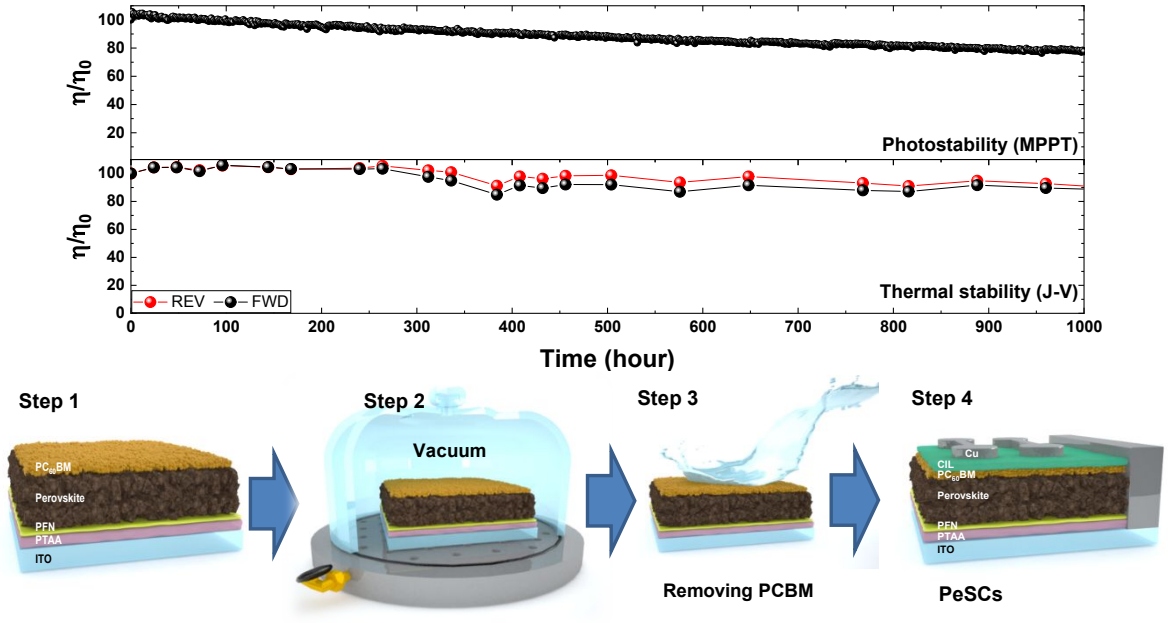

A long-term operational stability with 1000 hours in the inverted type perovskite solar cells based on the MAPbI3 layer is demonstrated in an ionic defect-free condition.